Optical Property Tuning of Single-Wall Carbon Nanotubes by Endohedral Encapsulation of a Wide Variety of Dielectric Molecules

Jochen Campo,[§] Sofie Cambré,[§] Bea Botka, Jan Obrzut, Wim Wenseleers,* and Jeffrey A. Fagan*

Cite This: https://dx.doi.org/10.1021/acsnano.0c08352

Read Online

ACCESS | Metrics & More | Article Recommendations | Supporting Information

ABSTRACT: Specific and tunable modification to the optical properties of single-wall carbon nanotubes (SWCNTs) is demonstrated through direct encapsulation into the nanotube interior of guest molecules with widely varying static dielectric constants. Filled through simple ingestion of the guest molecule, each SWCNT population is demonstrated to display a robust modification to absorbance, fluorescence, and Raman spectra. Over 30 distinct compounds, covering static dielectric constants from 1.8 to 109, are inserted in large diameter SWCNTs (d = 1.104−1.524 nm) and more than 10 compounds in small diameter SWCNTs (d = 0.747−1.153 nm), demonstrating that the general effect of filler dielectric on the nanotube optical properties is a monotonic energy reduction (red-shifting) of the optical transitions with increased magnitude of the dielectric constant. Systematic fitting of the two-dimensional fluorescence−excitation and Raman spectra additionally enables determination of the critical filling diameter for each molecule and distinguishing of overall trends from specific guest−host interactions. Comparisons to predictions from existing theory are presented, and specific guest molecule/SWCNT chirality combinations that disobey the general trend and theory are identified. A general increase of the fluorescence intensity and line narrowing is observed for low dielectric constants, with long linear alkane filled SWCNTs exhibiting emission intensities approaching those of empty SWCNTs. These results demonstrate an exploitable modulation in the optical properties of SWCNTs and provide a foundation for examining higher-order effects, such as due to nonbulk-like molecule stacking, in host−guest interactions in well-controlled nanopore size materials.

KEYWORDS: nanotube, single-wall carbon nanotube, optical characterization, dielectric constant, molecular packing, filling
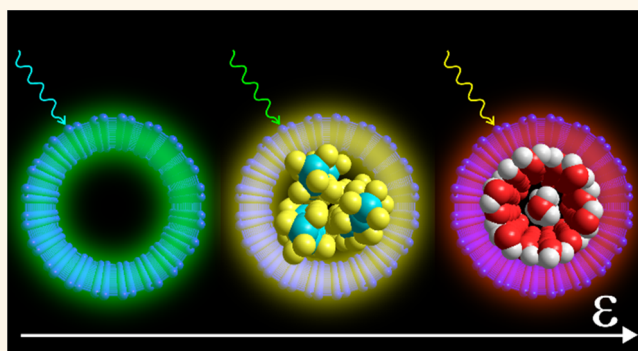
Single-wall carbon nanotubes (SWCNTs) are among the most studied of all nanomaterials due to their exceptional mechanical, electrical, thermal, and optical properties, making them ideal candidates for a wide range of applications.[1,2] Their actual implementation has, however, been strongly hampered by the complex polydispersity of the as-produced material with regards to the number and distribution of the individual chemical species, lengths, defect density, and impurity content.[3] Across the past decade plus, much effort has been put in developing schemes to reduce this polydispersity through various separation methodologies,[4−7] in particular for pure SWCNT species, colloquially termed "chiralities" and specified by chiral indices, n and m, denoting the "roll up" vector (n,m) of the nanotube's hexagonal carbon lattice. Most of these techniques require the SWCNTs to be dispersed in a solvent. However, most dispersion processes, for example, sonication, used to individualize SWCNTs, also tend

to cut nanotubes into shorter pieces with an additional consequence that the interior cavity is exposed to the solvent (*i.e.*, opening the SWCNTs).[8] Separately, chemical purification methods commonly used on commercial SWCNT materials to remove metallic catalytic particles and carbonaceous impurities also have a side effect of removing 100% of the end-caps of the nanotubes. Even in as-produced grade SWCNT powders, the natural abundance of empty SWCNTs after dispersion is typically low, <40%, and frequently <10%, although this can be

improved through furnace annealing.[8] Surprisingly given the ubiquity of open-ended SWCNTs in dispersed samples, solvent ingestion, for example, water ingestion during dispersion, is hardly discussed in the literature (except research on SWCNTs intentionally filled with specific molecules for achieving various functionalities).[9−12] For aqueous suspensions of SWCNTs in particular, it is very clear that water molecules spontaneously enter any open-ended SWCNTs,[8] and this uniformly for all chiralities, even down to the very smallest diameters present in the suspension, for example, the (5,3) species.[13]

Unfortunately, detailed investigations by optical spectroscopy have demonstrated that such water encapsulation broadens and shifts both the vibrational radial breathing mode (RBM) and optical transition energies of such water-filled SWCNTs compared to close-ended, "empty," SWCNTs and also causes a strong reduction in SWCNT emission efficiency.[8,13,14] This can be verified because separation of empty nanotubes from water-filled ones is possible on the basis of their density difference,[14,15] even for the smallest SWCNT diameters in which just a single row of molecules can be encapsulated.[16] Fortunately, the effect of water-filling on the RBMs also enables an efficient method for detecting the presence of closed (empty) and opened (water-filled) SWCNTs in aqueous suspensions.[8] Discrimination of an empty or water-filled nature can even be performed down to the level of individual SWCNTs through such measurements using single-particle imaging and spectroscopy.[17,18]

Separate from the advantageous filling by solvent of, generally undesirably, end-opened SWCNTs described above, there has been much interest in the incorporation of active molecules into nanotubes for use as electronic modulators,[9,19] as sources for the synthesis of unique materials,[20−22] and for drug delivery.[23−26] This research depends on the use of open-ended SWCNTs, and while filling procedures typically rely on high temperature and vacuum sublimation,[9,27−29] exceptions include encapsulation of photoactive molecules, such as sexithiophene,[30] β-carotene,[10] and a squaryllium dye[31,32] of interest for energy generation applications, and p,p′-dimethyl-laminonitrostilbene[12] for nonlinear optics. However, when such hybrid materials are processed via dispersion methods, or utilized for their optical properties, the retention of the filler can be questioned, requiring in particular detailed characterization of different modifications of the SWCNTs' optical properties (vibrational and electronic) of, for example, water- and solvent-filled SWCNTs with respect to the dye-filled SWCNTs noted above, to determine shifts characteristic for the encapsulant and to identify the minimal SWCNT diameter for encapsulation of the dye.

Because water-filling is so detrimental to many SWCNT optical properties, several of the authors recently realized and demonstrated a modification to the purposeful filling strategy noted above, namely, that a passive molecule could be used to fill the interior cavity of open-ended SWCNTs (as in active molecule filling) to prevent water encapsulation in a simple manner.[33] They demonstrated that controlled manipulation of the endohedral volume prior to dispersion, purification, and separation, particularly for the purpose of passivating the nanotube interior, can result in enhanced optical properties. Additionally, they were successful in encapsulating many alkane and alkane-similar compounds inside SWCNTs by simple immersion.[33] The much lower static dielectric constant of the alkanes ($\approx$2 at room temperature), as opposed to water,

resulted in nanotube optical properties closely resembling those of the empty SWCNTs but in sonicated, high-concentration, and macroscopic quantities.

Following this work, we now exploit the full potential of endohedral modulation to investigate the modulation possible through endohedral control. We apply the demonstrated, simple encapsulation procedure[33] (see Methods section) to a broad range of guest molecules covering bulk static dielectric constants, ε, from <2 to 109, and report on their effects on the optical properties of multiple host SWCNT diameter populations. By varying only the endohedral content of the SWCNTs and using a common exohedral environment, endohedral contributions to dielectric modulation are separately identified, and clear comparison to theory is enabled. As such, it is demonstrated that, overall, the optical transitions of the SWCNTs shift bathochromically upon increasing dielectricity of the filler molecule. This general dielectric screening effect is lasty found to represent only the "first-order" effect, with more specific host−guest interactions adding additional complexity to the observed SWCNT optical properties. These results in term enable the future quantitative deconvolution of "first-order" from "higher-order" effects for SWCNT−guest interactions and thus provide a foundation for this emerging area of SWCNT nanoscience.

RESULTS AND DISCUSSION

Filling the SWCNTs. Two different diameter distributions of opened SWCNTs were filled with a large number of different guest molecules following the procedure from Campo et al.,[33] that is, through simple immersion of the SWCNT soot in the neat liquid of the compound to be ingested. This was followed by filtration to remove the excess guest compound and typical processing via ultrasonication and subsequent ultracentrifugation to produce dispersions of isolated SWCNTs in aqueous sodium deoxycholate (DOC) solution. Full details are reported in the Methods section. Briefly, most guest molecules (22 of the 34) were incorporated in a "neat" fashion, that is, with no contact between the SWCNTs and other solvents prior to aqueous dispersion; in the remaining cases, an ethyl acetate (or in one case a methanol) rinse was required to remove solidified excess guest molecules (see Table S1 in the Supporting Information (SI)). For guest compounds that are solids at room temperature, these were added to the SWCNT powders and then heated in an oven to enable liquid-phase ingestion. For certainty, each SWCNT−guest pair was also contacted for a minimum of 18 h before filtering off of the excess, despite observations indicating that filling occurs near instantaneously in most cases (vide infra, Figure 3). Importantly, specific parent SWCNT sources, that is, soots, known to have opened end-caps were utilized for this work. As a source of larger diameter SWCNTs, commercial electric arc (EA) synthesis SWCNTs (Carbon Solutions, P2 grade; observable diameter range d = 1.104−1.524 nm), determined as the smallest and largest diameter yielding a measurable signal in PLE, vide infra, were utilized as received, while for smaller diameter SWCNTs, high-pressure carbon monoxide disproportionation (HiPco) SWCNTs (Carbon Nanotechnologies, Inc.; observable diameter range: 0.747−1.153 nm) were used, for which we assured fully open ends by applying a serial treatment of air oxidation, acid treatment, and annealing steps (see Methods section).[12] Table S1 reports all of the combinations of host SWCNT−guest molecules attempted as well as the processing specifics for each pair
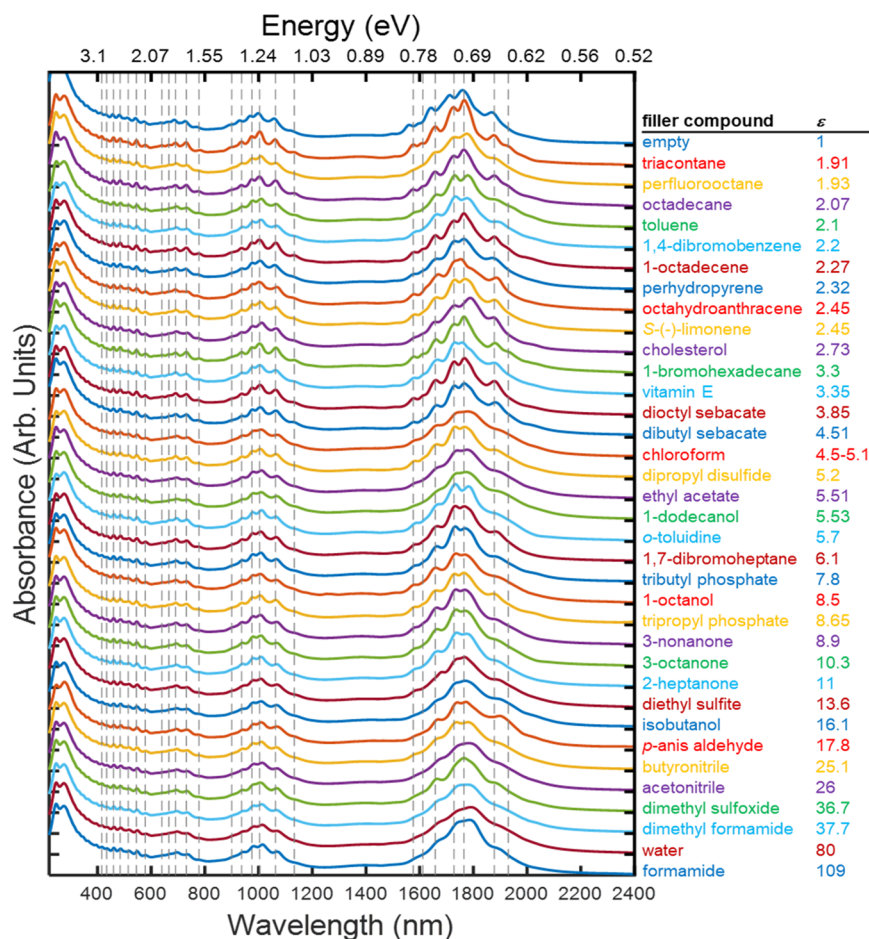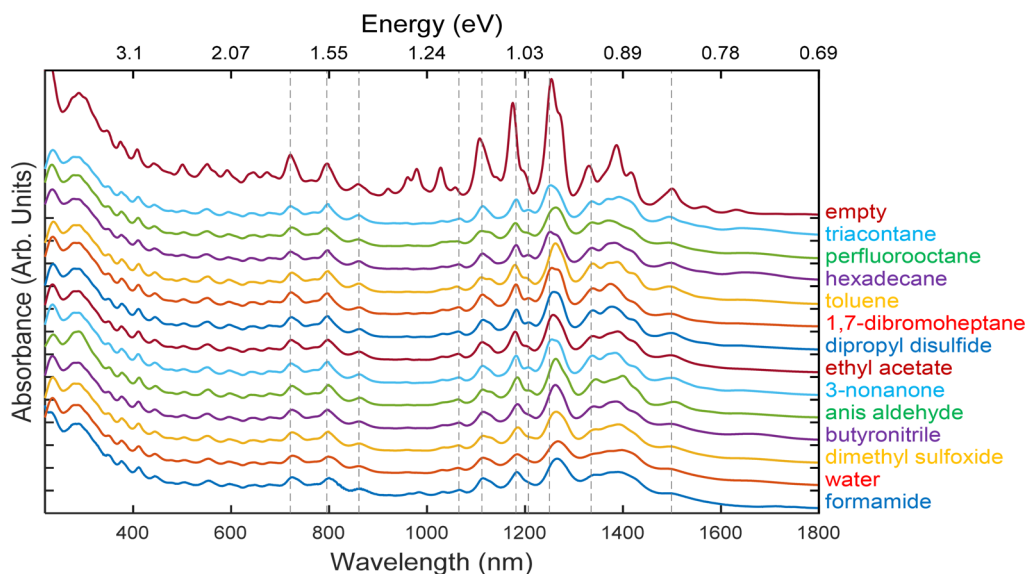
Figure 1. Absorbance spectra of empty, water-filled and all (34) guest@EA SWCNTs dispersed in 10 g/L DOC in D_2O. The different guest molecules clearly have characteristic effects on the electronic transitions of the host SWCNTs (see main text) visible in the line width and wavelength of the peaks. Spectra are presented in order of measured bulk static dielectric constant for the guest compound, increasing from top to bottom, and are normalized over the integrated E_{11}^S absorption (1400−2200 nm) with each spectrum offset by 1 arbitrary unit for clarity of comparison. Dashed vertical lines denote the peak wavelengths of selected optical transitions in the octadecane@SWCNT sample to provide visual reference for the shifts (and line broadening) occurring for the SWCNT populations with smaller and larger dielectric constant endohedral environments. Chemical structures of the different guest compounds can be found in Figure S1.

(guest and SWCNT) and experimentally determined static dielectric constants from the exact source lot of each guest compound. Figure S1 gives an overview of their chemical structures. Note that in the absence of controlled filling, both diameter distributions of nanotubes spontaneously fill with the dispersion solvent,[8,13] that is, water, during the dispersion process such that water-filled SWCNTs can be used as ideal reference samples. Note that heavy water, D_2O, is used for its optical transparency in the IR, but previous studies have demonstrated that the optical properties of H_2O-filled and D_2O-filled SWCNTs are equivalent. Following convention, the @ symbol is utilized herein to denote the guest molecule occupying the endohedral SWCNT volume, for example, triacontane inside EA SWCNTs: triacontane@EA SWCNT.

Absorption Spectroscopy. Optical absorbance spectra for all guest molecules @SWCNT as well as for the two reference samples containing empty (closed) and water-filled SWCNTs are reported in Figure 1 for EA SWCNTs and in Figure 2 for HiPco SWCNTs.

The absorbance spectra in Figures 1 and 2 represent all the measured guest@SWCNT samples, with a rich and equivalent distribution of optical transitions observed across all of the samples. Note that in addition to the regular ultracentrifuga-

tion typically applied after sonication to SWCNT dispersions to remove gross impurities, each of the guest@SWCNT populations (including the empty and water-filled populations) was further purified by application of an additional rate-zonal ultracentrifugation separation as previously developed for the bulk isolation of empty from water-filled SWCNT populations.[15] This separation greatly reduces the fractions of small residual bundles, kinked nanotubes, and dense impurities in the remaining population, enabling direct comparison of the absorbance of only highly individualized and well-dispersed guest@SWCNT populations. While the separation can in principle cause minor changes to the SWCNT population due to buoyancy differences, it is clear from Figures 1 and 2 that essentially no such changes have occurred, so that the relative peak positions, which are the measurand of import for establishing the modulation to properties, are only marginally affected. Importantly, also the quality of the absorbance spectra is indicative of well-dispersed SWCNTs in all cases, as demonstrated through high peak-to-baseline absorbance ratios and spectrally sharp features, denoting that the differences in guest molecule are not affecting the dispersion quality of the compared samples.
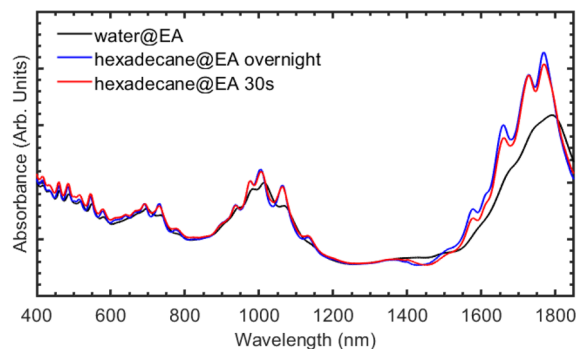
Figure 2. Absorbance spectra of empty, water-filled and 12 different guest@HiPco SWCNTs dispersed in 10 g/L DOC in D_2O. Spectra of filled SWCNTs are normalized over the integrated E_{11}^S absorption over the range of 880−1800 nm, with each spectrum offset by 1 arbitrary unit, for clarity. Note that the empty HiPco sample has a different diameter distribution as compared to the guest@HiPco SWCNT hybrids, as it necessarily originates from a different raw SWCNT material (see Methods section). Spectra are presented in increasing dielectric constant for the guest molecules from top to bottom, and dashed vertical lines represent the peak positions for the triacontane@SWCNT sample.

For the EA SWCNTs, from lesser to greater energy, sharp optical transitions relating to both the semiconducting SWCNT species E_{11}^S (approximate range 1500−2000 nm), E_{22}^S (900−1200 nm), E_{33}^S and E_{44}^S (450−600 nm) and metallic SWCNT species (E_{11}^M (600−800 nm)) are clearly visible as well as overlapping or weaker transitions such as E_{11}^S + phonon ($\approx$1250−1500 nm) and higher-order E_{ii}^S and E_{ii}^M transitions. In energy, shifts in the positions of the E_{11}^S and the corresponding E_{22}^S transitions due to the differences in internal guest molecule are of similar magnitude (*vide infra*), thus shifts in the peak positions are most noticeable for the E_{11}^S in Figure 1, but are apparent when zoomed in for all transitions. Demonstrably, spectra of each of the guest@SWCNTs are significantly sharper as compared to the water@SWCNT population, but slightly broadened with respect to the empty SWCNTs, and each of the guest@SWCNT samples displays red-shifted peak positions relative to the empty SWCNT sample, with the strong average trend across SWCNT species being an increasing red-shift with increasing bulk static dielectric of the filler molecule. Also, the optical transitions of the HiPco SWCNTs seem to exhibit significant variation with the guest dielectric. However, especially for smaller diameter SWCNTs, one must be careful to determine which CNTs are actually being filled as some of the guest molecules are too large to be confined in the smallest diameters (*vide infra*).

To demonstrate the ease and speed of the filling, Figure 3 compares the absorption spectra of EA SWCNTs immersed in hexadecane overnight or just for a very short $\approx$30s time. The excellent agreement between the two hexadecane@EA spectra demonstrates that filling actually occurs within seconds, demonstrating the importance of this study to the broad CNT community (as any solvents used in the processing of SWCNTs are likely to unintentionally fill them and modify their properties).

PLE Spectroscopy. Even though optical absorption spectroscopy yields a fast overview of optical effects from the

Figure 3. Absorbance spectra of hexadecane@EA SWCNTs obtained after overnight immersion in hexadecane (blue curve) or just a $\approx$30 s immersion (red curve), shown together with the spectrum of the water-filled EA SWCNTs (black curve). The very minor differences between the two hexadecane@SWCNT populations, and their equivalent differences from the water-filled sample, indicate that filling by alkanes (and likely most/all compounds) occurs very rapidly.

filling, it convolutes the contributions from all of the SWCNT (n,m) structures present in each population, preventing chirality-dependent shifts to be deduced. A more detailed evaluation of the spectral shifts of the electronic transitions of the guest@SWCNTs can be performed by means of two-dimensional (2D) infrared fluorescence−excitation (PLE) spectroscopy, which enables accurate identification of the peak positions from individual (n,m) structures *via* the 2D nature of this technique. PLE data were collected (see Methods section) for each of the guest@SWCNT samples as well as for the water-filled and empty SWCNTs. Afterward the PLE maps were calibrated for reabsorption by the nanotubes in the excitation and emission path and scaled by an estimated concentration of SWCNTs in each sample. The latter is important for comparison of the intensities only and does not affect quantification of the peak positions. The scaling was
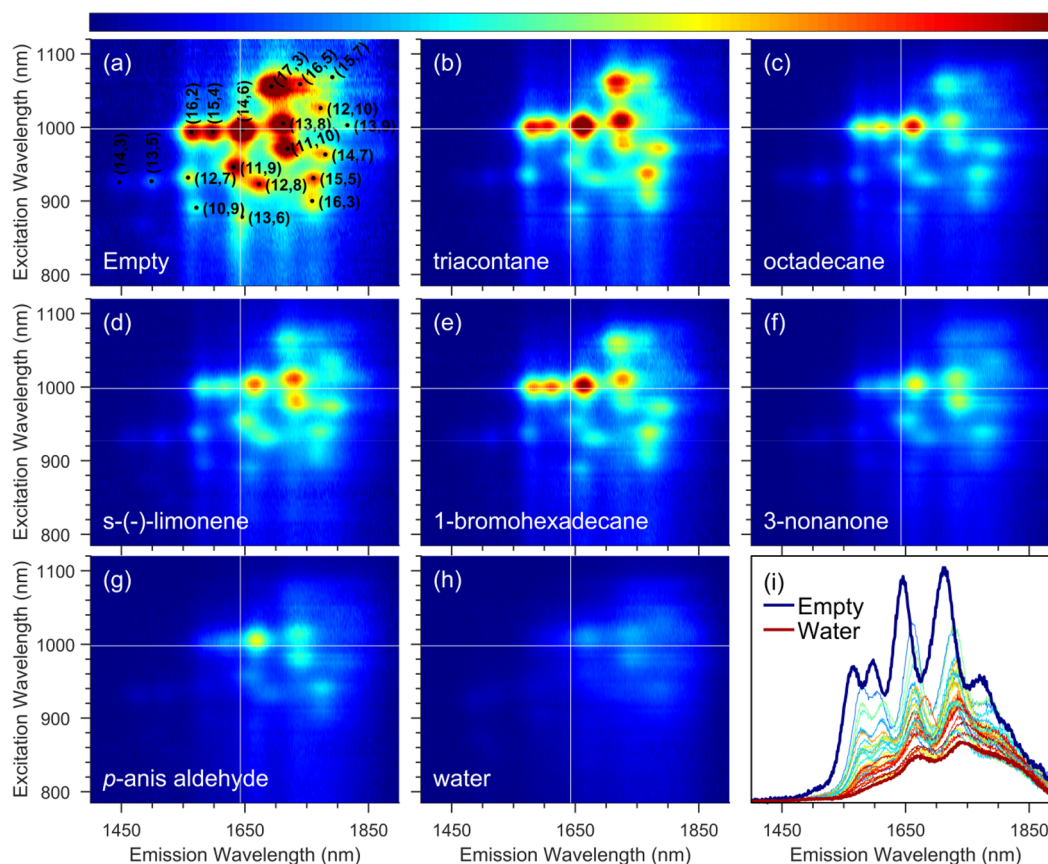
Figure 4. (a−h) The 2D PLE spectra for empty, water-filled and six representative guest@EA SWCNT samples, in order of increasing dielectric constant (full overview of all samples in Figure S4). Spectra are normalized for SWCNT concentration (see main text) and corrected for (re)absorption of the excitation and emission light so that intensities can be directly compared. Spectra of each of the guest@ EA SWCNTs and for the empty EA SWCNTs are significantly sharper and of increased intensity as compared to the water@EA SWCNT population. The white lines on the color maps indicate the peak position for the empty (14,6) SWCNT. The peak locations of the optical transitions of the SWCNTs are observed to monotonically increase in wavelength with the guest dielectric. (i) Relative intensities of the emission spectra integrated between excitation wavelengths from 970 to 1030 nm. For the color coding, the reduced dielectric constant of the filler is used, similar as in Figure 8, with the dark blue and dark red spectra corresponding to empty and water-filled SWCNTs, and all other fillers yielding intensities between these two extremes, showing on average a decreasing intensity for higher dielectric constants (see also Figure 13 and Figures S17 and S18).

done by first subtracting a 1/wavelength background from the absorption spectra as in Wenseleers *et al.*[34] and then integrating the absorption spectra over the E_{22}^S absorption range (*i.e.*, for 900−1200 nm EA SWCNTs and 485−918 nm for HiPco SWCNTs). Without subtracting the background, and directly integrating over the desired absorption range, this method results in very similar correction factors with only a 5% standard deviation in the ratio of the correction factors. Nevertheless, we opted to eliminate the background from the absorption first, to ensure that any residual non-SWCNT absorption in this background is removed when rescaling the PLE spectra. We furthermore want to stress that all samples were measured at a similar SWCNT concentration (scaling factors only differing within a 10% standard deviation) and that double checks were performed for these corrections, for example, by measuring the same sample several times or by diluting a sample by a known factor and remeasuring the PLE maps, both yielding reproducible results. The 2D color maps for water-filled and empty SWCNTs and a set of representative guest@SWCNTs for the EA and HiPco populations are shown in Figures 4 and 5, respectively (the remaining spectra are depicted in Figures S4 and S5).

Raman Spectroscopy. Similar as in Cambré *et al.*,[12] in addition to PLE, resonant Raman spectroscopy at various excitation wavelengths is applied in order to further demonstrate the internal filling for different guest molecules and to confirm any filler-specific threshold diameters for encapsulation. Indeed, the RBMs of the SWCNTs are very sensitive to the specific molecular structures encapsulated in the endohedral filling and are hence an excellent probe to investigate which SWCNT chiralities were successfully filled with the intended dielectric filler (and which ones are water-filled instead). While the PLE peaks directly represent the optical properties of the SWCNTs, the exact value of an RBM shift for a specific guest molecule will depend on the steric resistance those molecules provide in the compression−expansion of the SWCNT breathing mode and hence yields highly complementary information. Investigating the RBMs is particularly interesting for the guest@HiPco SWCNT hybrids, as in contrast to the EA SWCNTs, the HiPco SWCNTs contain SWCNTs with a too-narrow diameter to viably encapsulate many of the investigated fillers and can therefore reveal molecule-specific threshold SWCNT diameters for successful filling.
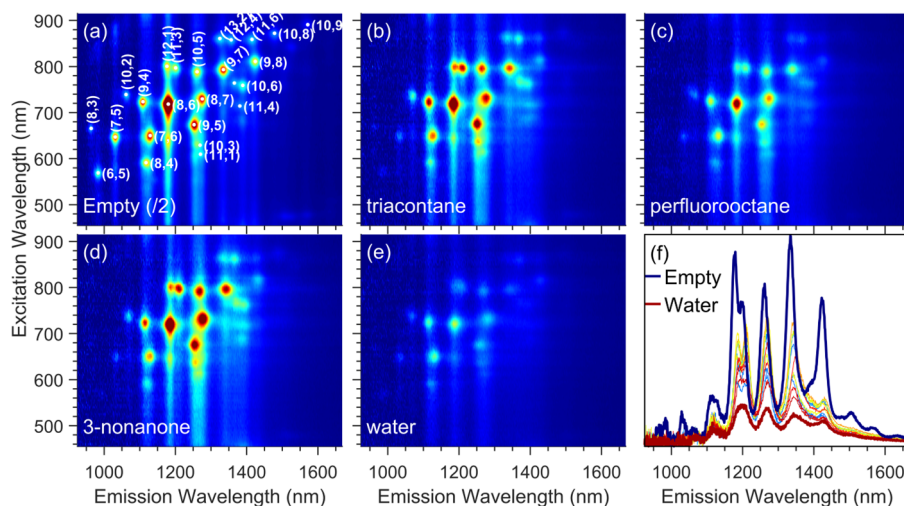
Figure 5. (a−e) The 2D PLE spectra for empty, water-filled and three representative guest@HiPco SWCNT samples, in order of increasing dielectric constant (full overview of all samples in Figure S5). Spectra are normalized for SWCNT concentration (see main text) and corrected for (re)absorption of the excitation and emission light so that intensities can be compared. (f) Comparison of one-dimensional slices for all the different samples, integrated for the excitation wavelength range from 780 to 820 nm. For the color coding, the reduced dielectric constant of the filler is used, similar as in Figure 8, with the dark blue and dark red spectra corresponding to empty and water-filled SWCNTs. Spectra of each of the guest@HiPco SWCNT populations and for the empty HiPco SWCNTs are sharper and of increased intensity as compared to the water@HiPco SWCNTs. Overall, the peak locations of the optical transitions of the SWCNTs are observed to monotonically increase in wavelength with the guest dielectric. Note that the empty HiPco sample has a different diameter distribution as compared to the guest@HiPco SWCNT hybrids, as it necessarily originates from a different raw SWCNT material (see Methods section), and its fluorescence intensity (here divided by two in the PLE maps) can therefore not be directly compared to that of the filled SWCNTs (see also Figure S5 for the PLE maps for other fillers).

Figure 6a,b presents the Raman spectra of all guest@HiPco SWCNTs obtained at two different laser excitation wavelengths (Raman spectra of HiPco and EA SWCNT samples at other excitation wavelengths are summarized in Figures S6−S9). The spectral shifts of the RBM signals for the different guest@HiPco samples can be directly observed by comparing the spectra against those of the empty and water-filled SWCNTs and can be quantified by determining the positions of the RBMs by multi-Lorentzian fitting. Unless otherwise noted, uncertainties in this manuscript are reported as values equal to ±1 standard deviation.

Two examples of such an analysis are shown in Figure 6c,d, which summarize the processing of the Raman data for the perfluorooctane and 1-bromohexadecane@HiPco SWCNT hybrids. In Figure 6a, it is clearly seen that the RBMs of the perfluorooctane-treated (9,7), (10,5), (11,4), and (8,7) SWCNTs are shifted compared to those of their empty and water-filled counterparts (hence these SWCNT chiralities are assigned as perfluorooctane-filled), while those of the narrower diameter (11,3), (12,1), (9,4), and (10,2) SWCNTs show RBMs at the same frequencies and line widths as the water-filled chiralities (hence they are water-filled), clearly demonstrating a critical diameter for filling with perfluorooctane approximating that of the (8,7) SWCNT. This is more directly seen in Figure 6c, which summarizes the RBM peak shifts of the perfluorooctane@HiPco versus the D_2O@HiPco SWCNTs as a function of diameter and clearly shows the onset of perfluorooctane filling by the suddenly nonzero values for diameters larger than ≈1.018 nm ((8,7) SWCNT (diameters were calculated using a carbon−carbon distance in the graphene lattice of 0.142 nm). Similarly, for 1-bromohexadecane (Figure 6b,d), SWCNT chiralities with diameters smaller than ≈0.903 nm (the (9,4) SWCNT) do not show any shift with respect to the water-filled SWCNTs (hence these are

water-filled), while larger diameter tubes show clear RBM shifts with respect to water-filled SWCNTS. Since the shift of the RBM is related to the steric interaction of the SWCNT wall with the encapsulated molecules, that is, inducing a counteracting force on the RBM vibration, the observed shifts with respect to water-filled tubes can be both positive (showing a larger RBM frequency, stronger interaction) or negative (smaller RBM frequency, smaller interaction), but with respect to empty SWCNTs, shifts are always toward higher frequency. Since RBM shifts with respect to water-filled SWCNTs are very small, these characterizations can of course only be performed for well-isolated SWCNTs, resulting in narrow line widths of the RBMs. Along with the RBM spectral shift, guest@SWCNT RBMs are typically also narrower than those of water-filled SWCNTs, which can be observed when simultaneously comparing RBM shifts and RBM line widths, as presented in Figure S8. Furthermore, we found the threshold for observation of a nonwater RBM shift to correlate very closely with the characteristic theoretical cross-section of each encapsulated molecule and that the absolute value of the RBM shift was similar for molecules with similar minimal cross-section projections. Indeed, when comparing the RBMs of triacontane@ versus hexadecane@HiPco SWCNTs (Figure 7), for which the cross-section remains identical and only the length of the chain changes, RBM peak positions are identical, demonstrating that the observed RBM shifts with respect to water-filled SWCNTs are not random but related to the specific size and stacking of the encapsulated molecules. Lastly, when necessary, systematic comparisons of the RBM peak positions were also made against an ethyl acetate@SWCNT reference sample, to ensure that the rinsing solvent did not replace the intended filler during the washing procedure (see Methods section).
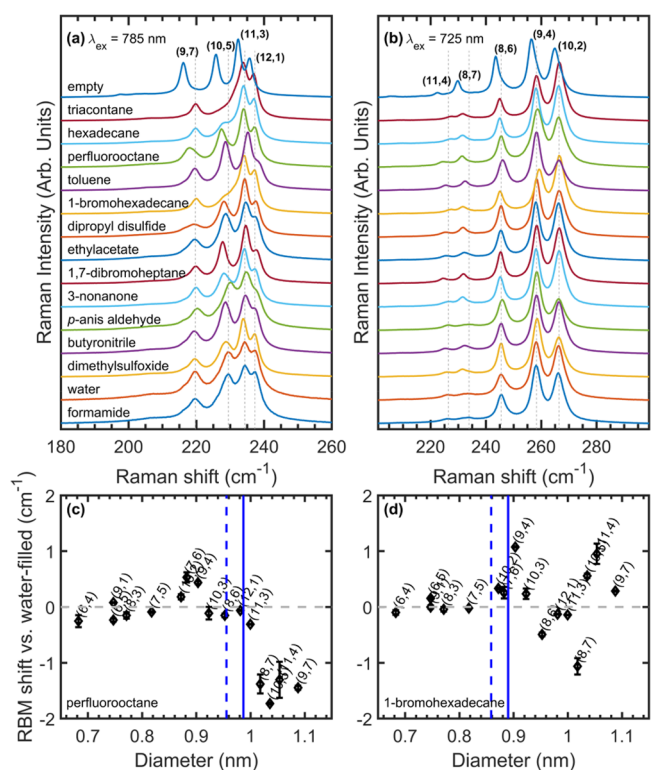
Figure 6. (a,b) Resonant Raman spectra of empty, water-filled, and all other guest@HiPco SWCNTs, excited at 785 nm (a) and 725 nm (b). RBM peak positions are obtained by multi-Lorentzian fitting of the spectra and are compared to the RBM positions of water-filled SWCNTs, by plotting the shift of the RBM frequency as a function of SWCNT diameter (c) for perfluorooctane-filled SWCNTs and (d) 1-bromohexadecane-filled SWCNTs. While larger diameter SWCNTs show clear shifts of the RBM peak positions with respect to water-filled SWCNTs (hence these chiralities are filled with the guest molecule), those of the narrower SWCNTs are at the same (or very similar) frequency (hence water-filled), clearly demonstrating a critical diameter for filling. A full overview of such figures for all samples can be found in Figure S7. The dashed line indicates the calculated critical diameter for filling by perfluorooctane, whereas the solid line takes into account the fixed offset on this value based on ref 12. Error bars represent 1-σ uncertainties as obtained from the fitting procedure.

Minimal Encapsulation Diameter. For comparison, we computationally estimated the critical filling diameter by first optimizing the structure of the encapsulated molecules in vacuum using quantum-chemical calculations at the Hartree–Fock level with the semiempirical Hamiltonian PM7 (as implemented in MOPAC)[35] and subsequently calculating the cylinder with minimal diameter surrounding this optimized molecular structure, taking into account standard van der Waals radii[36] and adding twice the van der Waals radius of the SWCNT carbon atoms (taken to be half the interlayer spacing of graphite, i.e., 0.1677 nm) to account for the inner van der Waals surface of the SWCNT. The experimentally observed minimal encapsulation diameter is very consistent with the minimal diameter estimated as such (highlighted by the dashed blue line in Figures 6 and 7 and Figure S7), especially when an empirical offset based on our previous study using p,p′-dimethylaminonitrostilbene[12] (i.e., 0.0313 nm) is taken into account (solid lines in Figures 6 and 7 and Figure S7). Note that these thresholds are calculated for the minimal energy static diameter of each molecule and do not consider distortion
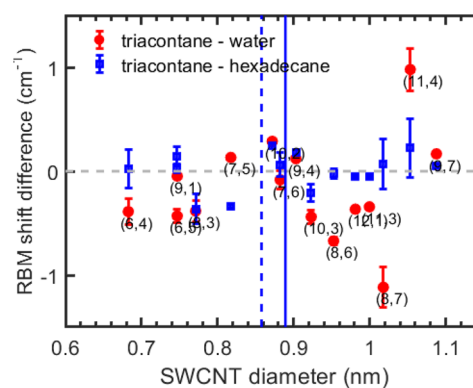
Figure 7. Spectral shifts of the RBMs of triacontane SWCNT hybrids with respect to water-filled (red) or with respect to hexadecane-filled (blue) SWCNTs, plotted as a function of SWCNT diameter. The dashed line indicates the calculated critical diameter for a relaxed linear alkane structure, see text, whereas the solid line takes into account an empirical offset on this value based on our previous study using p,p′-dimethylaminonitrostilbene.[12] While the RBM frequencies of triacontane-filled SWCNTs are clearly shifted with respect to water-filled SWCNTs, the shifts with respect to hexadecane-filled SWCNTs are much smaller (negligible for most chiralities).

of the molecule (or the SWCNTs)[37] or fluctuations in shape due to thermal energy that may enable encapsulation. Regardless, within the HiPco diameter range, critical filling diameters were observed based on the RBM shifts (Figure S7) for many filler molecules, each within good agreement of the calculated values when including the common offset. The guest@EA SWCNTs always showed clear spectral shifts of their RBMs relative to their water-filled counterparts (see, e.g., Figure S9), demonstrating endohedral filling, but these exact shifts are hard to determine accurately in this case due to a strong overlap between the different RBM peaks. In any case, all EA SWCNTs are sufficiently large to encapsulate all the various molecules used in this study.

In summary, whether or not a specific (n,m) was successfully filled by the desired guest molecule and its effects on the SWCNT optical properties were determined by several spectroscopic methods. In the following discussion *it is important to note that we only discuss SWCNT chiralities for which the PLE peak positions could be fitted reliably and that correspond to SWCNTs that are undoubtedly filled with the intended guest molecule.* This means that we purposely exclude some guest and species combinations that may fill under optimized circumstances. To make this selection, that is, to determine which chiralities were effectively filled with the applied guest molecule (for reasons of critical filling diameter) and to check for fillers which might not have worked for any chirality, be it due to unsuccessful encapsulation to start with, possible stochastic or partial filling, or exchange with water during aqueous solubilization, we make extensive use of the complementary combination of resonant Raman data and their multi-Lorentzian fits (as in Figures 6 and 7) and PLE data sets (see, e.g., Figure S12), where we compare both peak positions and line widths, and for PLE also intensities of the presumably filled SWCNTs against the water-filled SWCNTs. In addition, the experimentally determined critical filling diameters are compared to the theoretical ones. While these different pieces of information by themselves often yield the same conclusion on whether intentional filling occurred, sometimes this is not
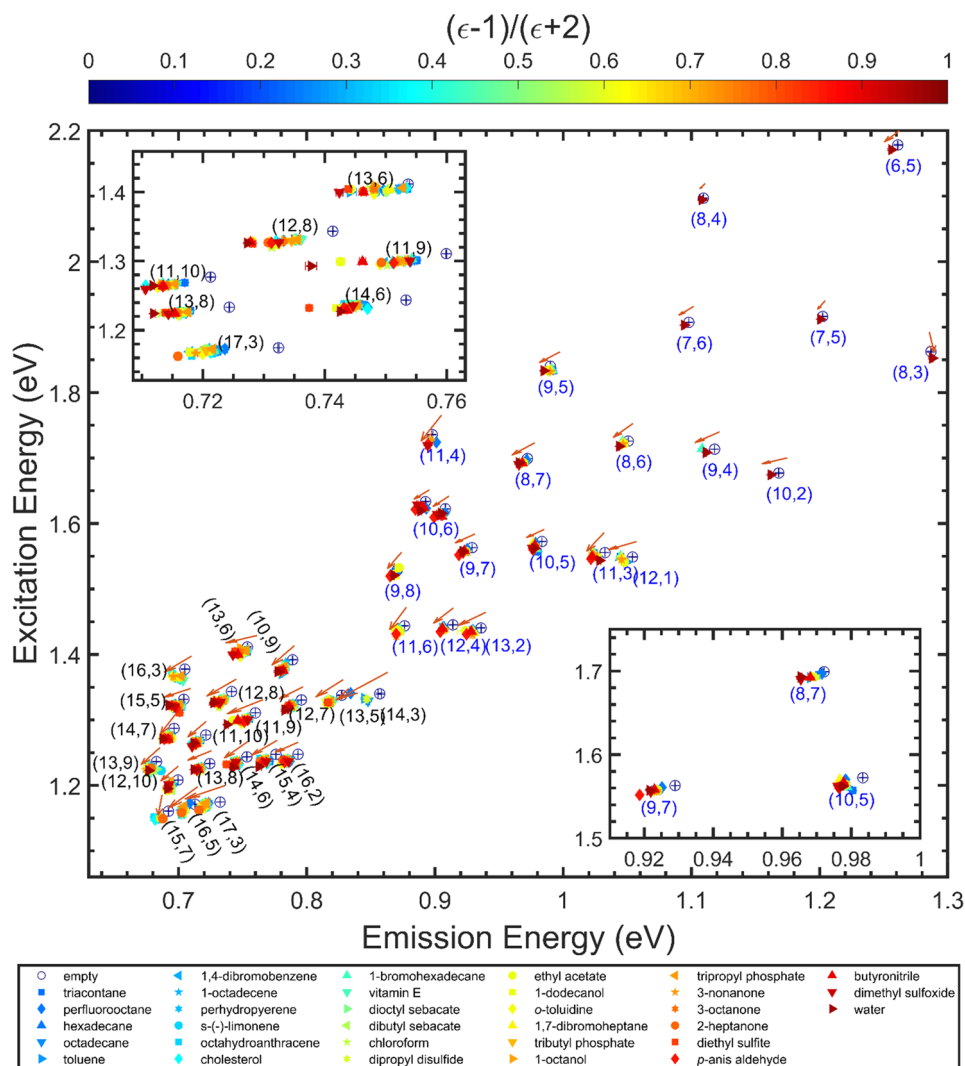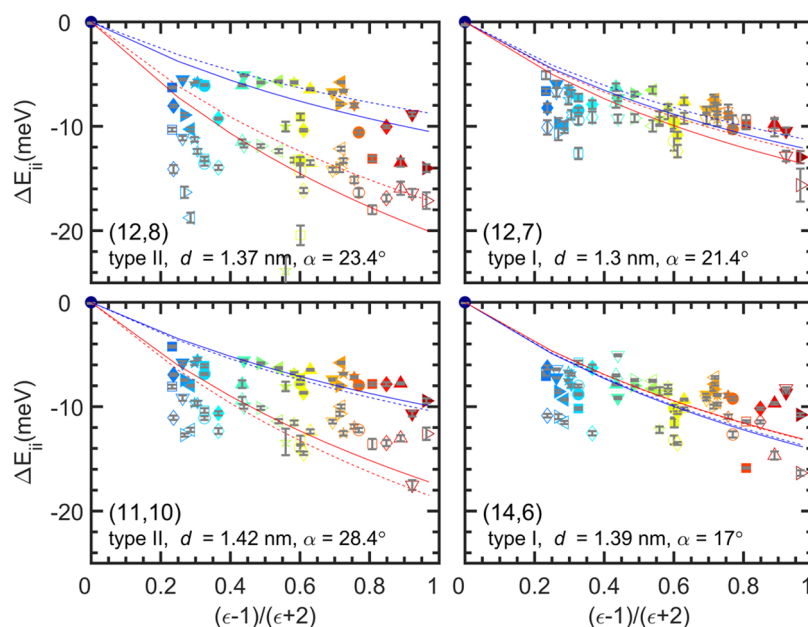
Figure 8. Overview of the PLE peak positions for the different guest@SWCNT (*n,m*) species, as obtained from the 2D fitting procedure (tabulated data is presented in the SI). Only those peak positions that could be reliably fit and that correspond to SWCNTs that are considered to be filled with the intended filler through combined Raman and PLE analysis (*vide supra*) are included. The depicted arrows point from low toward high dielectric constants (*i.e.*, connecting the points corresponding to a reduced dielectric constant of 0 (vacuum) and 1 (limit of high polarity), as obtained from a linear fit to the peak positions as a function of reduced ε (as in Figure 9), and subsequently magnified three times for clarity), and (*n,m*) labels in black (blue), respectively, indicate SWCNT chiralities corresponding to the EA (HiPco) SWCNT populations. Empty peak positions are given as open blue circles, and error bars are 1-σ errors obtained directly from the fitting program. For each chirality, peak positions are overall monotonically red-shifting proportional to the dielectric constant of the filler molecule (color-coded from blue to red, as shown by the color bar at the top of the figure), as also clearly seen in the zoomed-in insets. Across chiralities, the spectral shifts with respect to endohedral polarity increase significantly and gradually toward larger diameter SWCNTs. Note that the apparent crosses in the empty points reflect the uncertainties in the energy values, which are very small compared to the effect of the filler variation.

the case. For instance, different conclusions can be drawn from the different sources of information for some SWCNTs close to the diameter threshold or for highly polar fillers, for example, those for which the PLE peak positions of the filled SWCNTs could be expected to be similar to water-filled SWCNTs. In those cases, it is crucial to rely on the combination of all data. In particular, for isobutanol, acetonitrile, and dimethylformamide (DMF), each of which is a small polar molecule, only three to four chiralities displayed significant shifts in E_{11} in PLE measurements (see Figure S12), and hardly any changes were observed for the other parameters (RBM shift, line widths). Similarly, for formamide, PLE peak positions, RBM peak positions, and PLE and RBM line widths did not yield a clear indication of filling,

excepting a somewhat greater PLE intensity from the formamide-filled population as compared to water-filled SWCNTs as an indication of filling. However, as this intensity increase was only minor ($\approx$30%, see Figure 13), we cannot conclusively state that this filling was successful. It is evident that for these highly polar fillers, the differences with the water-filled SWCNTs are very small, making it difficult to conclusively assign a SWCNT as successfully filled. However, on the other hand, these fillers are highly soluble in water and thus could be exchanged with water molecules during the dispersion of the SWCNTs (potentially nonuniformly across the various (*n,m*) species), similar to what was observed for dye-filled SWCNTs dissolved in a solvent in which the dye is soluble.[32] Therefore, for all certainty, these fillers (*i.e.*,

Figure 9. Spectral shifts of the E_{11} (solid symbols) and E_{22} (hollow symbols) PLE peak positions (relative to the empty SWCNTs; $\Delta E_{ii} = E_{ii}(\text{filled}) - E_{ii}(\text{empty})$) for four SWCNT species, serving as representative examples (full overview in Figure S13). The chiral indices, the SWCNT type (*i.e.*, $(2n + m)$ mod 3), diameter, and chiral angle are presented in each panel. The shifts correspond to the data shown in Figure 8 and are here plotted as a function of reduced dielectric constant of the filler (color- and style-coded as in Figure 8). The ΔE_{11} and ΔE_{22} data points follow largely the same trends and are fitted using the model presented in eq 1 either by fitting this equation to the data of each chirality separately (*i.e.*, blue and red solid lines for ΔE_{11} and ΔE_{22}, respectively) or by adding eq 2 as an additional condition for the fits and fit all chiralities simultaneously (blue and red dashed lines for ΔE_{11} and ΔE_{22}, respectively). Shifts are generally increasing (*i.e.*, increasingly strong redshift) toward larger dielectric constants. The overall trend is superimposed with more subtle "higher-order" variations which can be attributed to specific stacking effects due to the molecule's cross-section (*vide infra* Figure 12).

isobutanol, acetonitrile, DMF, and formamide) were omitted from the following discussion. Lastly, while previously some of the authors have reported filling of SWCNTs as small as the (6,5) chirality with linear alkanes under optimized preparation,[37] such species show a split RBM peak for these fillers in this work (see Figure S6a), which could be interpreted as successful filling of only part of the population. In view of the current purpose of revealing the effect of dielectric constant on the optical properties of SWCNTs, these data points were therefore also omitted from the experimental data.

Electronic Shifts. To accurately determine the peak positions, line widths, and amplitudes for the intrinsic SWCNT peaks, the PLE maps of Figures 4 and 5 (and Figures S4 and S5) were fitted using an empirical 2D fitting model (see SI, section S8). This model is an adaptation of the previously developed fitting routine[12] and is based on an accurate description for the complicated excitation line shape associated with both excitonic and band-to-band excitations as well as phonon side bands for the SWCNTs. The peak positions obtained as such, and taking into account only those chiralities that are considered filled with a specific filler (see above) for both the EA and HiPco SWCNT populations, are summarized in Figure 8.

Figure 8 contains a wealth of information on the filler-specific effects on the optical properties of the host SWCNTs. It is, for example, clearly seen that for each SWCNT chirality, the peak positions are generally bathochromically shifting with increasing dielectric constant of the endohedral molecule, both in E_{11} and E_{22}. To visualize this more in detail, the energy shifts for a few representative example chiralities are plotted as a function of the dielectricity of the encapsulated molecules in Figure 9 (full overview in Figure S13). Note that rather than

opposing the data against the refractive index at optical frequencies, they are plotted *versus* the (static) dielectric constant (ε). The effects observed here are indeed expected to be correlated with the refractive index at the (IR) frequency corresponding to the exciton binding energy, and hence within good approximation, are well-represented by the value measured for the static dielectric constant (permittivity in the DC limit). Moreover, in particular, here we use the "reduced" dielectric constant, that is, $(\varepsilon - 1)/(\varepsilon + 2)$, which is mainly done to visually spread the points for low dielectric constant guest molecules at which the effects of changing interior dielectric are expected to be most significant. Tabulated data for the emission energies as a function of filler and SWCNT species reported in Figure 8 are provided in the SI.

Note that differences between the empty SWCNTs and their filled counterparts other than being filled or not, such as additional defects in the opened/filled SWCNTs, doping of the filled SWCNTs, or strain exerted by the encapsulated molecules on the SWCNTs, can be ruled out by comparing the Raman spectra and in particular the D- and G-bands (see Figure S16). Indeed, no significant difference is observed in the G/D ratio of all samples (notably a high G/D ratio of $\approx$145 was consistently obtained, evidencing the high purity of the samples), and no significant shifts of the G-band can be observed (any shifts observed are smaller than 1 cm^{-1}).

Comparison to Existing Theoretical Models. To model the experimentally observed shifts of the optical transitions, we first compare our experimental data to the theoretical model previously developed by Miyauchi *et al.*[38] In this study, the optical transition energies of SWCNTs are calculated using a screened Coulomb potential with a net dielectric constant "κ"

that is approximated as a linear combination of the screening by the nanotube itself (κ_{tube}) and the surrounding material (ε) ($\kappa^{-1} = C_{tube}\kappa_{tube}^{-1} + C_{env}\varepsilon^{-1}$). This then turns into the following fitting model for the electronic shifts (eq (11) in Miyauchi *et al*):[38]

$$\Delta E_{ii} = E_{ii}^{filled} - E_{ii}^{empty} = \frac{-A_{nm}(\varepsilon - 1)}{\varepsilon(\kappa_{tube}^{\infty} - \kappa^{vac}) + 1/\kappa^{vac}} \quad (1)$$

where κ_{tube}^{∞} is the value of the net dielectric constant κ for infinite external dielectric constant ε ($\kappa(\varepsilon \to \infty)$) and κ^{vac} is the value of the net dielectric constant κ for vacuum ($\varepsilon = 1$). The value of κ^{vac} is assumed to be equal to 1.5 in Miyauchi *et al*.[38] and in the same work ($\kappa_{tube}^{\infty} - \kappa^{vac}$) was found to be roughly proportional to the inverse SWCNT-diameter squared with the proportionality factor equal to 1.5 nm^2. Thus, the electronic shifts are expressed as a function of external dielectric constant (ε) with a single fitting parameter A_{nm} for each chiral structure (n,m), corresponding to the gradient of the curves at small dielectric constant.

Figure 9 shows that this model (solid lines) can nicely reproduce the overall trend observed in the experimental data (fits for other chiralities can be found in the Figure S13). Miyauchi *et al*.[38] furthermore also predict that the fitting parameters A_{nm} should display specific family patterns (*i.e.*, for $2n + m =$ constant) and should follow (to a first approximation) the following diameter and chirality dependence (eq (12) in Miyauchi *et al*):[38]

$$A_{nm} = A + Bd + (C + D/d)\cos 3\theta \quad (2)$$

where (d,θ) is the diameter and chiral angle of the SWCNT and A, B, C, and D are the parameters that depend on the modulus of the SWCNT. To test this dependency, instead of fitting the different A_{nm} for each chiral structure (n,m) separately (solid lines in Figures 9 and S13), we also performed a simultaneous fit for all chiralities which are filled with more than two fillers, with the above condition for A_{nm} and thus with the parameters (A,B,C,D) as sole fitting parameters. The so-obtained fits are depicted as dashed lines in Figure 9 and Figure S13 and were obtained by following fitting parameters: for ΔE_{11}, the obtained parameters were 11.6 ± 2.1 meV, −3.2 ± 1.5 meV nm^{-1}, 3.6 ± 1.7 meV, 4.5 ± 3.1 meV nm and 14.2 ± 2.4 meV, −4.3 ± 1.8 meV nm^{-1}, 12.7 ± 2.3 meV, −30.2 ± 4.3 meV nm for type I (here defined as [($2n + m$) mod 3 = 1]) and type II ([($2n + m$) mod 3 = 2]) SWCNTs, respectively, and for ΔE_{22}, the best fit was obtained with 21.5 ± 3.9 meV, −7.6 ± 2.8 meV nm^{-1}, 0.6 ± 2.9 meV, −2.6 ± 5.4 meV nm and 7.8 ± 5.3 meV, 4.4 ± 3.8 meV nm^{-1}, −12.8 ± 5.6 meV, 24.4 ± 10.7 meV nm for type I and type II SWCNTs, respectively.

Overall, even this simultaneous fit reproduces quite well the overall trend with increasing dielectric constant that is observed experimentally, despite the simplicity of the model and the fact that eq 2 is only a first-order approximation to the theoretical values. Note that the experimental A_{nm} values found here (and plotted in Figure 10) are at least a factor of 2 smaller than those found in reference Miyauchi *et al.*,[38] which can be explained by the fact that the model was derived for externally surrounding dielectric media and not for encapsulated ones, as also theoretically found by Ando.[39] Indeed, for SWCNTs externally surrounded by solvents with different dielectric constants, much larger shifts up to 100 meV were experimentally observed by Silvera-Batista *et al.*[40] In addition,
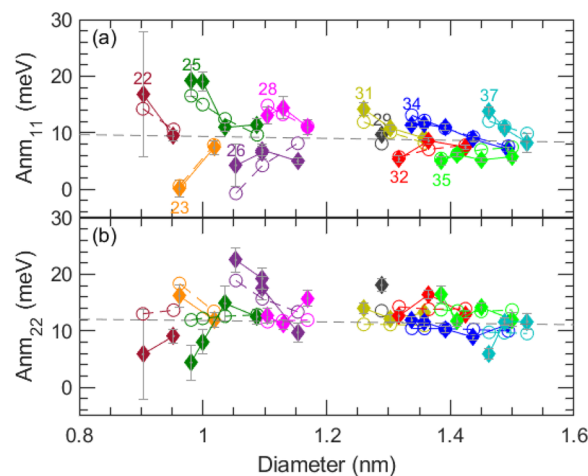

Figure 10. Family patterns ($2n + m$) for the fitted A_{nm} values for first (a) and second (b) optical transitions of the SWCNTs *versus* SWCNT diameter (fits shown in Figure 9 and Figure S13). Each family is presented in a different color, as indicated by the colored numbers in (a). The filled diamonds correspond to the unconstrained fits to eq 1 for each chirality separately, while the opened circles denote the values for the constrained simultaneous fits including also eq 2. The filled diamonds nicely follow the predicted family pattern (open circles), in particular for ΔE_{11}. Type I and type II SWCNTs are inverted with respect to the gray dashed line for ΔE_{11} *versus* ΔE_{22}. Overall, a weak diameter dependence can be observed, as indicated by the gray dashed line, and in agreement with theoretical calculations.[38]

we observe a similar gradual diameter dependence of the A_{nm} values decreasing toward larger diameters (indicated by the gray line in Figure 10). The largest deviations between the two fits (dashed and solid curves) can be found for SWCNTs with relatively small chiral angles (*e.g.*, (11,3), (12,1), and (13,7)), but the overall conclusion is that our experimental data also follow the expected family patterns (as can be also observed in Figure 10). Indeed, similarly as in the theory, we observe that type II SWCNTs show a larger dependence on chiral angle (*i.e.*, larger parameters C and D) as compared to type I SWCNTs. In contrast, however, for ΔE_{11}, the sign of the experimental D parameter is negative, while positive in the theory, hence resulting in an inverted behavior of the branches with respect to the gray dashed line in Figure 10. Note also that our experimental data show that for ΔE_{22}, the signs of the C and D parameters also invert with respect to ΔE_{11}, which was not investigated in Miyauchi *et al.*[38]

To further investigate the chirality- and diameter-dependent behavior, we also compare our experimental data to the theoretical models of Jiang *et al.*[41] and Ando.[39] By solving the Bethe−Salpeter equation within a tight-binding approach, Jiang *et al.*[41] previously calculated the shift of the optical transition energies of SWCNTs when embedded in an external dielectric environment as a function of diameter and chiral angle. To model the dielectric screening, an "arbitrary" constant κ was introduced in the Coulomb potential to incorporate both the screening by the nanotube itself and by the external dielectric material. Therefore, the constant "κ" cannot be directly related to dielectric constant of the external medium, making it more difficult (as opposed to the results of Miyauchi *et al.*[38] described above) to compare these theoretical predictions to our experimental values.
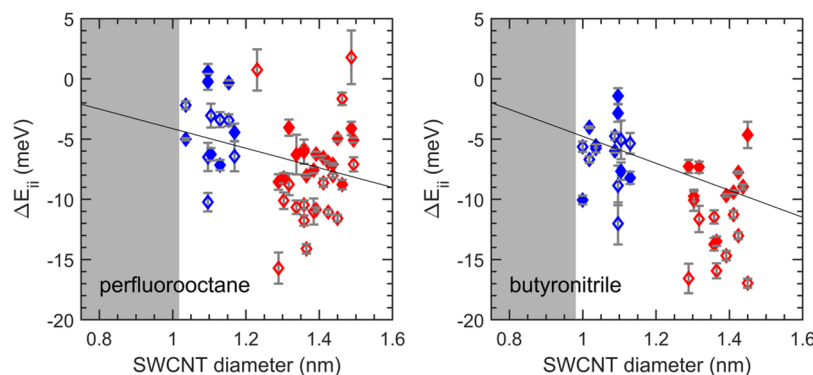
Figure 11. Spectral shifts of the E_{11} (solid symbols) and E_{22} (hollow symbols) PLE peak positions (relative to the empty SWCNTs; $\Delta E_{ii} = E_{ii}(\text{filled}) - E_{ii}(\text{empty})$) for two fillers (that were encapsulated in both the HiPco and EA SWCNT populations; serving as representative examples (full overview in Figure S14)), plotted as a function of SWCNT diameter. The shaded area represents the SWCNT diameters that are not filled. In each case, an increasingly strong redshift is observed toward larger diameters, with a smooth transition from HiPco to EA SWCNTs (HiPco and EA chiralities are depicted in blue and red, respectively). A linear fit to the E_{11} and E_{22} data (black solid line) is shown as a guide-to-the-eye.

A first observation we make in agreement with Jiang *et al.*[41] is that the absolute shift in energy $|\Delta E_{ii}|$ of the second optical transitions is always larger or equal to the shift of the first optical transition. In our experiments (*e.g.*, Figure 9 and Figure S13), we indeed find almost universally $|\Delta E_{22}| \geq |\Delta E_{11}|$, in agreement with this theory, with a few exceptions such as the (11,3) and (12,1) chirality. A second theoretical prediction by Jiang *et al.* is that there should be a family behavior to the shifts of the electronic transitions, where for E_{11}, type II tubes are predicted to typically have larger absolute shifts $|\Delta E_{11}|$ than type I tubes, and additionally they find that this trend is reversed for the second optical transitions.[41] Combined with the previous finding, type II tubes should have much smaller differences between $|\Delta E_{22}|$ and $|\Delta E_{11}|$ than type I tubes. Interestingly, in our experimental data set, however, we observe the exact opposite (see Figure 9 and Figure S13), where for type II tubes, the differences between $|\Delta E_{22}|$ and $|\Delta E_{11}|$ are much larger than for type I tubes. Finally, Jiang *et al.* also predict a tube diameter dependence, which for an external medium is that the above effects are largest for the smallest diameters.[41] In Figure 11, we plot the spectral shifts of the E_{11} and E_{22} transitions as a function of SWCNT diameter, for a representative distribution of filler molecules (full overview in Figure S14). In every case, in contrast to the theoretical prediction, the absolute redshift is found to increase toward larger SWCNT diameters, with moreover a rather continuous transition from the HiPco to the EA SWCNTs. The latter excludes a significant dependence on the SWCNT raw material used, which *a priori* was not at all obvious considering the SWCNT material's different synthesis methods and origins.

The above discrepancies of our experimental results with these theoretical calculations with respect to the different behavior of type I and II SWCNTs most likely originate from the fact that the theoretical models are based on the interaction of the SWCNTs with an external dielectric medium, and our experimental data hence hint that an adaptation of these models, for example, in the description of the interaction potential, will be needed for the description of endohedral filling with dielectric materials. The larger shift upon filling for larger SWCNT diameters can be ascribed to the fact that for these larger SWCNTs, the volume fraction of the internal volume of the tube that gets filled up by the guest compound is larger than for smaller diameter SWCNTs (also taking into

account the van der Waals radius of the SWCNT carbon atoms and the actual space that can be filled up), which has indeed been theoretically predicted to lead to increasing energy shifts using a continuum model by Ando.[39]

Empirical Relations for E_{11} and E_{22}. In Bachilo *et al.*,[42] empirical relations were determined to predict the PLE peak positions of semiconducting SWCNTs. Here, we have determined the parameters of these empirical relations for several of the studied fillers by directly fitting simultaneously the experimental PLE maps of EA and HiPco SWCNTs with one set of empirical relations. To this end, we replaced the parameters determining the peak positions of each chirality (*i.e.*, E_{11} and E_{22}) by the empirical relations, and we simultaneously fitted the EA and HiPco SWCNT PLE maps to provide the required broad diameter distribution. Note that in this way also chiralities with only very weak PL intensity can be included in the fitting and that the number of fitting parameters is drastically reduced from 104 fitting parameters (E_{11} and E_{22} from 52 chiralities) to just 8 parameters of the empirical relations. We furthermore included also the minimal encapsulation diameter determined before into these fits, such that chiralities with diameters below this minimal encapsulation diameter were fitted with the empirical relations of water-filled SWCNTs. By fitting the PLE maps directly with the empirical relations, the parameters of these relations and their respective errors correctly take into account the weight of each contributing SWCNT chirality's signal in the fitting by their relative amplitudes. Example fits are presented in the SI, section S12 and Figure S20. Interestingly, also the parameters of these empirical relations clearly show a dependence on the dielectric constant (see Figure S21). The parameters of these empirical relations for all fillers that are encapsulated in both HiPco and EA samples are provided in the Table S2.

Comparison of Different Fillers. Of great interest, we can demonstrate that superimposed on the general trend induced by the endohedral dielectric, more subtle molecule (n,m)-specific variations occur in some cases, which could be attributed to molecular stacking effects. The large variety of filler molecules investigated allows us to compare subtly different fillers (with very similar dielectric constants and molecular shape) for checking the origin of the superimposed variations of the shifts. For instance, we can compare, for the case of similar fillers, linear alkanes of different lengths (*i.e.*,
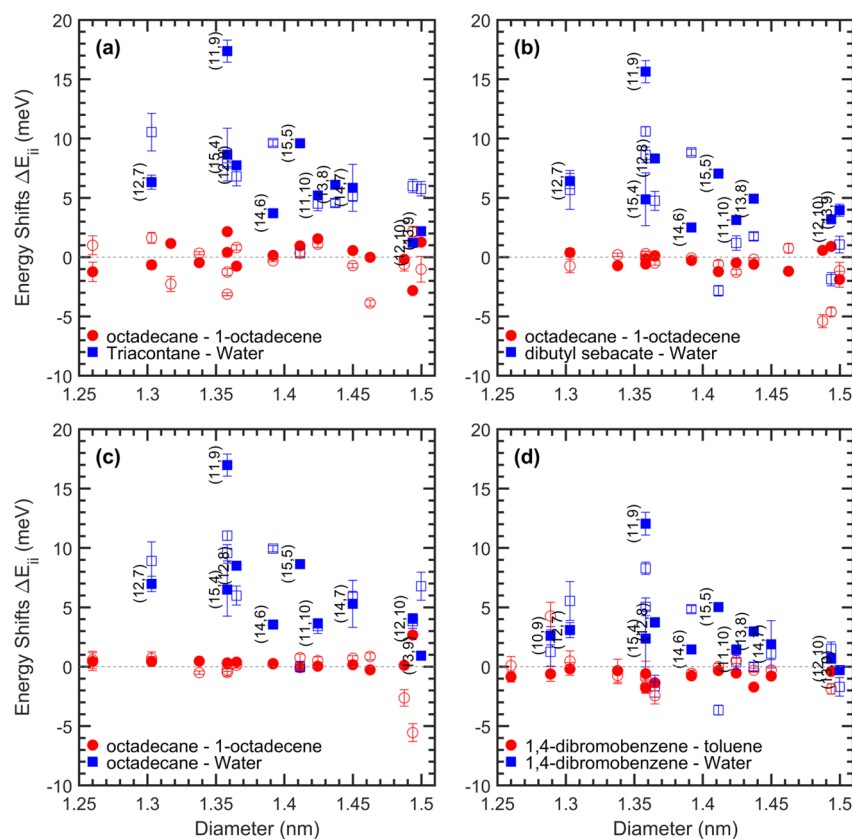
Figure 12. Spectral shifts of the E_{11} (solid symbols) and E_{22} (hollow symbols) PLE peak positions of the SWCNTs filled with (a) triacontane relative to octadecane (red symbols), that is, $\Delta E_{ii} = E_{ii}(\text{triacontane}) - E_{ii}(\text{octadecane})$, for comparison shown together with the shifts of the triacontane-filled SWCNTs with respect to their water-filled counterparts (blue symbols); $\Delta E_{ii} = E_{ii}(\text{triacontane}) - E_{ii}(\text{water})$. Similar plots but comparing (b) dibutyl sebacate with dioctyl sebacate, (c) octadecane with 1-octadecene, and (d) 1,4-dibromobenzene with toluene. Interestingly, while the filling of each of these dielectrics yields markedly different PLE peak positions compared to water filling, in general no measurable differences are observed among the sebacates or alkanes mutually, or among linear alkanes and alkenes, or mono- or disubstituted aromatic compounds, indicating that in this case, the subtle differences in molecular structure do not lead to drastic differences in molecular packing upon confinement in the SWCNTs, and in fact demonstrate the excellent reproducibility of the PLE peak positions under repeated sample preparations.

octadecane *versus* triacontane; Figure 12a), the sebacates (*i.e.*, dioctyl sebacate *versus* dibutyl sebacate; Figure 12b), one of the linear alkanes *versus* the alkene (*i.e.*, octadecane *versus* 1-octadecene; Figure 12c), mono- *versus* disubstituted aromatic compounds (*i.e.*, toluene *versus* 1,4-dibromobenzene, Figure 12d), *etc.* Interestingly, no significant differences are observed in any of those cases, indicating that the subtle differences in molecular structure do not lead to drastic differences in molecular packing upon confinement in the SWCNTs and, as such, demonstrating the excellent reproducibility of the PLE peak positions under repeated sample preparations.

Such a comparison can also be made for the Raman data, for example, the RBM shifts of the HiPco SWCNTs filled with hexadecane can be compared with those filled with the longer triacontane molecules. As the sole difference between these two linear alkanes is their chain length, their critical filling diameter should be the same, and in particular their effect on the RBM frequency is expected to be very similar, which is indeed what is observed here (see Figure 7 above). Characteristically, however, less subtle molecular structure variations do result in significant and often large differences in PLE peak positions, especially when the structure change results in a different dielectric constant (*e.g.*, 1-octanol *versus* octadecane, toluene *versus* o-toluidine, triacontane *versus* dipropyldisulfide *etc.*) or for fillers with similar dielectricity

but quite different size, as is the case for perfluorooctane *versus* triacontane (Figure S15). Distinctively, perfluorooctane is an example filler molecule that violates the overall trend of PLE peak shifts *versus* dielectric constant, as can indeed be seen in the plots for the different chiralities in Figure 9 and Figure S13. A potential explanation is that while the dielectric constant of perfluorooctane is very similar to that of the hydrogenated linear alkanes, its refractive index is much lower (1.3 *versus* 1.44). This implies that its polarizability at optical frequencies is significantly different, which could result in altered effects on the optical properties of the surrounding SWCNTs, and hence be at the origin of this observation. An alternative explanation could be that nanoconfinement of the significantly larger fluorinated alkane as compared to the hydrogenated case leads to differences in molecular stacking, causing different perturbations on the host SWCNTs. Extraction and characterization of single enantiomer samples of single SWCNT species, as has only recently been accomplished in the larger diameter regime,[43] which would enable additional measurement precision, may be necessary to resolve this question.

PL Quantum Efficiency. Finally, in addition to shifts of the PLE peak positions, the relative intensities of the emission peaks from the guest@SWCNT dispersions can be examined as a function of the internal dielectric. A first approach is to compare aggregate intensity at normalized solution concen-
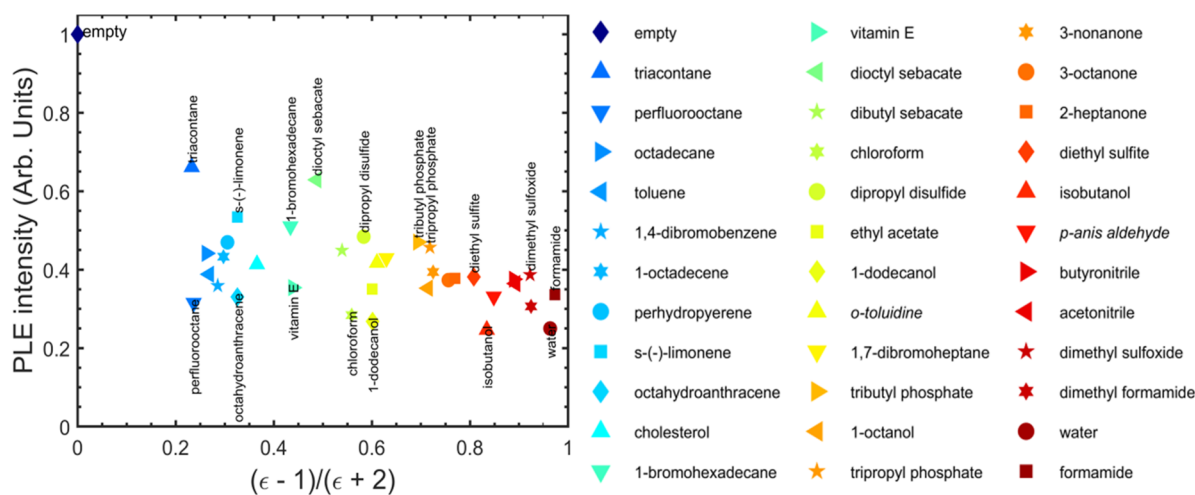
Figure 13. Relative PL intensities calculated *via* integration of the intensity over the excitation and emission ranges in the PLE maps from Figure 4 and Figure S4 of the guest@EA SWCNTs, as a function of reduced dielectric constant of the guest molecule (color- and style-coded as in Figure 8). A general increase from water toward low polarity fillers is clearly observed, reaching the highest fluorescence intensity for triacontane filling. While the filled EA SWCNTs can be compared because of their very similar diameter distributions (as seen in the absorption spectra in Figure 1, and the PLE maps in Figure 4 and Figure S4), a comparison with the corresponding empty SWCNTs needs to be done taking into account that they originate from a different starting SWCNT sample. Note that for the intensities of the individual chiralities, as obtained by the PLE fit, the effect of the different fillers can be very different from chirality to chirality (see full overviews in Figures S17 and 18).

tration by integrating over the full PLE maps shown in Figure 4 and Figure S4. The result of this analysis is shown in Figure 13. In Figure 13, it is seen that overall the PLE intensity increases substantially from water-filling with a reduction in the polarity of the filler molecule, reaching the highest intensity for triacontane filling. Deviations from this general trend however are observed, for example, for perfluorooctane, which yields a much lower PL intensity than other guest@SWCNT populations with similar dielectric constant materials (*e.g.*, triacontane). At a finer level, a comparison of the emission intensity for several SWCNT (*n,m*) species separately can be found in Figures S17 and S18. While the magnitude of the dependence of the PLE intensity on the dielectricity of the filler varies strongly from chirality to chirality, low polarity fillers mostly result in the highest intensity, approaching that of the corresponding empty SWCNT. Note that for the comparison to the PL of the empty SWCNTs, it should be kept in mind that these originate from a different batch of SWCNTs, *i.e.*, that did not undergo the opening procedure, and so the absolute comparison may be affected by factors of average SWCNT length or carbon lattice pristineness in addition, and unrelated to, the filling difference.

CONCLUSIONS

In this work, the internal cavities of SWCNTs of widely different diameters were filled with well over 30 different compounds, with widely varying dielectric constants from 1 to 109. Every specific guest molecule that fits inside an (*n,m*) is found to have characteristic effects on the optical transitions of the SWCNTs, as observed in both absorption and 2D infrared PLE spectroscopy. At the level of individual SWCNT chiralities, an overall, monotonous bathochromic shift of the optical transitions is generally observed with increasing dielectricity of the encapsulated molecule, along with more subtle higher-order variations attributable to molecular stacking effects. For each filler molecule, the magnitude of the redshift is found to increase toward larger SWCNT

diameters, as is the slope of the linear dependence of the shifts *versus* dielectric constant. Moreover, we demonstrate unambiguously that the fluorescence intensity of the nanohybrids generally decreases toward higher dielectric constant filler molecules, an effect that appears to be accompanied by line width broadening.

Dependencies of the electronic shifts on the specific optical transition (E_{11} *versus* E_{22}) and family behavior of the SWCNTs were also determined and strikingly turn out to be opposite with respect to the existing theoretical models for externally changing dielectric environment. Importantly, before such determinations were made, the endohedral filling was additionally evidenced and further investigated by multiwavelength resonant Raman spectroscopy. This allowed the observation of critical filling diameters for different compounds, demonstrating agreement with calculated filling diameters, and to exclude nonfilled nanotubes from corrupting the data set and the theoretical comparisons. With this enhanced validation, the large experimental data set provided here is thus particularly valuable for future model development and description of endohedrally dielectrically modulated SWCNTs.

Moreover, many of the studied fillers are commonly used in SWCNT research, and it is important to realize that even a short exposure to these molecules can unintentionally fill the SWCNTs and thus modify their properties. We further impart value by generating empirical relations as derived in Bachilo *et al.*[42] for the first- and second-transition frequencies for a few fillers, as these provide further ease of use for future research efforts. Hence, through the analysis of a vast spectroscopic data set comprising a wide variety of host SWCNT/guest molecule combinations, this work reveals this facile, controllable, and predictable way to modulate and enhance the optical properties of SWCNTs, by filling their internal channel with molecules of varying and well-chosen dielectricity.

METHODS

Certain equipment, instruments, or materials are identified in this paper in order to adequately specify the experimental details. Such identification does not imply recommendation by the National Institute of Standards and Technology (NIST) nor does it imply the materials are necessarily the best available for the purpose.

Purified electric arc (EA) synthesized single-wall carbon nanotube soot, P2 grade, lot no. 02-A011 (acquired in 2015), was acquired from Carbon Solutions (Riverside, California) and used as received. Purified HiPco soot from Carbon Nanotechnologies Inc. (CNI), lot no. P0257 *circa* 2005, was further processed by a multistep air oxidation, acid wash, and annealing process described before[8,12,44] to ensure all nanotubes were fully open-ended and without residual endohedral contaminants. Empty EA SWCNTs were extracted from Carbon Solutions raw AP-grade SWCNT soot (lot no. A218, 2015) using rate-zonal ultracentrifugation.[15] As the purified CNI HiPco soot contains virtually no empty SWCNTs, empty HiPco SWCNTs were obtained from NoPo HiPco soot (NoPo Nanotechnologies), by rate-zonal ultracentrifugation (as in Fagan *et al.*[15]) followed by isopycnic density gradient ultracentrifugation (as in Cambré *et al.*[14]). In order to increase the yield of empty SWCNTs, the soot was solubilized without tip sonication and with just a limited dose of bath sonication. The filling procedure for liquid guest molecules consisted of a simple immersion of a known mass of SWCNT powder in a small volume of the guest liquid (see Table S1 for the processing specifics for each guest liquid/SWCNT soot pair). For guest molecules in the solid phase at room temperature, a quantity of the solid sufficient to fully wet the SWCNT soot was added to the soot, and the closed vials were incubated above the melting temperature of the solid. In both cases, the soot and liquid were contacted for a minimum of 18 h, although separate results indicate filling likely occurs within seconds (see Figure 3). Note that caution should be used in the choice and handling of guest chemicals and proper personal protective equipment utilized at all times. Filtration was used to remove the bulk of the liquid from contacted SWCNT powders and to rinse off molecules residing at the outside of the SWCNTs. Millipore membranes VVLP, 0.1 μm pore size, and FG type, 0.2 μm pore size, membranes were used in a stainless steel filter holder (Whatmann) for this task. Liquids with sufficient vapor pressure were expressed simply by the application of air from a hand-held syringe, while other liquids and solidified compounds were removed by pushing a solvent, typically ethyl acetate, through the exposed soot followed by air to express the wash solvent (see Table S1). Filtered soot, typically forming a solid cake/bucky paper, was subsequently taken out of the filter holder and allowed to dry in a fume hood. Some samples with low vapor pressure guest molecules were heated to 50−60 °C to expedite the drying process. Nominal drying of the sample is generally necessary to prevent competition for micellar encapsulation by the surfactant molecule during dispersion.

Filled SWCNT materials were dispersed into a 20 g/L filtered (0.1 μm) sodium deoxycholate solution *via* tip sonication as previously reported. Briefly, soot and surfactant solution were sonicated in 12−40 mL volumes depending on the sample at ≈1.0 mg/mL SWCNT concentration (EA SWCNTs) or ≈0.8 mg/mL (HiPco SWCNTs) at ≈0.9 W/mL nominal applied power with a 6.35 mm (1/4 in.) tip probe sonicator for 1 h. For a 35 mL volume of pure water, the measured power output of this tip was found to be ≈50% of the nominal power. After sonication, the resulting rough dispersions were purified by centrifugation, collecting the supernatant: Beckman JA-20 rotor at 1882 rad/s (18 kRPM, ≈ 40 kG at maximum radius) for 2 h, Beckman SW-32 rotor at 2304 rad/s (22 kRPM) for 2 h, or Eppendorf 7500 342 rotor at 2094 rad/s (20 kRPM) for (30 to 60) min, depending on the amount of sample and instrument availability.

To further isolate solely the individualized, well-dispersed, guest@SWCNT fraction of each population, each sonicated and centrifuged dispersion was additionally purified by rate-zonal ultracentrifugation against a step density gradient as previously described (additional details in SI). After rate-zonal separation, the dispersions of purified, individualized, guest@SWCNT were dialyzed *via* pressurized stir-cells

(Millipore) with either 30 kDa or 100 kDa regenerated cellulose membranes to remove the density gradient media and then for exchange into final 10 g/L DOC in D$_2$O solution.

Absorbance measurements were performed on a CARY 5000 UV−visible near-infrared spectrophotometer at a slit bandpass of either 1 or 2 nm in 0.5−1 nm steps and an integration time of 0.1 s/step with a 100% T baseline and separate measurement of the surfactant solution without nanotubes as a reference. Measurements were made in 1 mm path length quartz cells. All measurements were performed at room temperature.

Fluorescence measurements were performed on two instruments. NIR fluorescence for the narrowest HiPco SWCNTs was measured on a Horiba Jobin Yvon Nanolog-3 spectrofluorometer with a liquid nitrogen cooled InGaAs array detector and a 450 W xenon lamp. Excitation was selected using a dual grating monochromator with 1200 grooves/mm × 500 blaze, nm gratings and a slit selected bandpass of 5 nm. Emission was measured in the right-angle geometry with a 2 mm × 10 mm quartz cuvette through a long-pass filter and dispersed with a 100 grooves/mm and blaze 800 nm grating onto the array detector. Bandpass for the emission side was set to 5 nm. Integration time at each excitation wavelength was 30 s (contour plot). Collected spectra were corrected for the wavelength-dependent irradiance of the excitation beam, and the wavelength dependence of the long pass filter and detector train (including grating) was calibrated using a NIST traceable lamp. Temperature of the cell was controlled using a temperature controller (Quantum Northwest model TLC 50) set to 20.00 °C, and samples were each equilibrated for ≈5 min before measurement.

NIR fluorescence for the broader HiPco and the EA SWCNTs was collected using an in-house developed dedicated spectrometer consisting of a pulsed xenon lamp (Edinburgh Instruments, Xe900-XP920) for the excitation and a liquid-nitrogen cooled extended InGaAs array detector (Princeton Instruments OMA V:1024) sensitive up to 2.2 μm. Spectra were recorded in 90° geometry in a 3 mm microcell, with 5 nm steps in excitation wavelength. Excitation wavelengths were selected with a 300 mm grating monochromator (Acton SpectraPro 2355) equipped with a 1200 gr/mm grating, and emission spectra were analyzed using a 150 mm grating spectrograph (Acton SpectraPro 2156) equipped with a 150 gr/mm grating, resulting in a slit-selected instrumental resolution of 8 nm in excitation and 10 nm in emission wavelength. All PLE maps were corrected for detector and spectrograph efficiency, filter transmission, and spectral and temporal variations of the excitation intensity and were corrected for (re)absorption of the excitation and emitted light so that intensities can be compared. In addition, PLE maps were normalized over SWCNT concentration, which was obtained by first subtracting a 1/wavelength background from the absorption spectra, and then integrating the absorption spectra over the E$_{22}$ wavelength-range.

Raman spectra were collected in backscattering geometry using a Dilor XY800 Triple spectrometer equipped with a liquid nitrogen cooled CCD detector. An Ar$^+$, Kr$^+$, and tunable Ti:sapphire laser were used for resonant excitation of the different SWCNTs. Individual spectra were corrected for detector and spectrograph efficiency and obtained with subwavenumber spectral resolution. To accurately determine the spectral shifts of the RBMs of the guest@HiPco SWCNT hybrids, these spectra were fitted using a sum of Lorentzian profiles. The RBM frequencies of the empty and water-filled SWCNTs were determined by simultaneous fitting of these two data sets, and the optimized parameters for the water-filled SWCNTs were then used as starting values to fit the guest@HiPco SWCNT spectra. Weak contributions from residual empty SWCNTs were added in a few cases, in the form of Lorentzian profiles with frequency and width fixed as determined for the empty SWCNTs, but with freely varying amplitude. To determine the static dielectric constants of the different guest compounds, complex impedance (Z^*), capacitance (C), and resistance (R) measurements were carried out at 20 °C in the frequency range from 40 Hz to 30 MHz using an Agilent 4294A Precision Impedance Analyzer configured for the 4-terminal test fixture. Liquid specimens were measured using 16452A

Liquid Test Fixture from Agilent in accordance with the Operation and Service Manual for 16452 A. The measurements were done with a gap between electrodes of 0.5 mm to obtain capacitance of the empty cell (C_0) in the range of 20 pF. Solid films were measured in a parallel plate capacitor configuration made of two boron-silicate glass slides with 12 mm diameter circular electrodes. Gold electrodes, 100 nm thick, were deposited on plasma-cleaned surfaces over 1 nm titanium layer using a shadow mask and vacuum evaporation. Approximately 0.2 mm-thick spacers were attached to the glass slides and used to control the gap between the top and bottom electrodes such that the capacitance (C_0) of the empty (air filled) test fixture was about 10 pF. Solid film specimens were prepared by melting samples between glass slides with electrodes, contacts, and spacers clamped together. Before measurements, the test fixture was compensated to an electrical short, open, and a 100 Ω load according to the fixture extension procedure specified by the manufacturer for the 4294A impedance analyzer. The organic materials characterized in this work show a primary relaxation at frequencies above 100 MHz, and therefore, the sample capacitance (C_S) is assumed to be frequency independent in our experimental frequency range. However, due to residual impurities and electrode polarization (EP) effects, several solvents show an increase in the experimental capacitance at the lowest frequencies, and thus obscuring the C_S value. Typically the electrode polarization capacitance (C_{EP}) was extracted from the measured capacitance (C) by the frequency variation technique described by Schwan[45] or from a distributed equivalent RC circuit model for EP impedance, as described in Emmert *et al.*[46]

The real part of the relaxed (static) dielectric constant was obtained from the ratio of the sample capacitance (C_S) divided by capacitance of the empty cell $\varepsilon_S' = C_S/C_0$. We note that several high dielectric constant solvents showed abnormally high dielectric increment ($\Delta\varepsilon_{EP}$) values from EP polarization and a peak in the dielectric loss $\varepsilon_S'' = 1/(2\pi f R C_0)$ located in the sub kHz frequency range. In such cases, we determined ε_S' from a distributed equivalent RC circuit model for EP impedance and by fitting C_S/C_0 to the Debye relaxation formula.[46] The combined relative uncertainty in ε_S' is 4%. The results are shown in Table S1.

ASSOCIATED CONTENT

Ⓢ Supporting Information

The Supporting Information is available free of charge at https://pubs.acs.org/doi/10.1021/acsnano.0c08352.

Chemical structures and a table summarizing all the combinations of host SWCNT−guest molecules attempted, measured and literature reported dielectric constants for the guest compounds, photographs of the filling procedure, details of the rate-zonal separation, complete set of PLE maps for guest@EA and guest@HiPco SWCNTs, additional resonance Raman scattering data for guest@EA and guest@HiPco samples, details on the applied 2D PLE fitting procedure and examples of the 2D fits, detailed overview figures analyzing the shifts and line broadening upon filling, G- and D-band Raman spectra of guest@EA samples, PL intensity of guest@EA and guest@HiPco for different chiralities (PDF)

Numerical values of the PLE peak positions and line widths for the different fillers obtained from 2D fits (XLSX)

AUTHOR INFORMATION

Corresponding Authors

Jeffrey A. Fagan − *Materials Science and Engineering Division, National Institute of Standards and Technology, Gaithersburg, Maryland 20899-8542, United States;* ● orcid.org/0000-0003-1483-5554; Email: Jeffrey.Fagan@ nist.gov

Wim Wenseleers − *Department of Physics, University of Antwerp, B-2610 Antwerpen, Belgium;* ● orcid.org/0000-0002-3509-0945; Email: Wim.Wenseleers@ uantwerpen.be

Authors

Jochen Campo − *Materials Science and Engineering Division, National Institute of Standards and Technology, Gaithersburg, Maryland 20899-8542, United States; Department of Physics, University of Antwerp, B-2610 Antwerpen, Belgium;* ● orcid.org/0000-0002-5198-2302

Sofie Cambré − *Department of Physics, University of Antwerp, B-2610 Antwerpen, Belgium;* ● orcid.org/0000-0001-7471-7678

‖**Bea Botka** − *Department of Physics, University of Antwerp, B-2610 Antwerpen, Belgium*

Jan Obrzut − *Materials Science and Engineering Division, National Institute of Standards and Technology, Gaithersburg, Maryland 20899-8542, United States;* ● orcid.org/0000-0001-6667-9712

Complete contact information is available at:
https://pubs.acs.org/10.1021/acsnano.0c08352

Author Contributions

§These authors contributed equally to this work.

Notes

The authors declare no competing financial interest.
‖Present Address: Wigner Research Centre for Physics, 29-33 Konkoly-Thege M. Rd, 1121 Budapest, Hungary

REFERENCES

(1) Zhang, Q. *Carbon Nanotubes and Their Applications*; CRC Press: New York, 2012.

(2) Iijima, S.; Ichihashi, T. Single-Shell Carbon Nanotubes of 1-nm Diameter. *Nature* **1993**, *363* (6430), 603−605.

(3) Dresselhaus, M. S.; Dresselhaus, G.; Avouris, P. Carbon Nanotubes. *Topics in Applied Physics*; Jorio, A., Dresselhaus, G., Dresselhaus, M. S., Eds.; Springer:Berlin, Heidelberg, 2001; Vol. *111*.

(4) Arnold, M. S.; Green, A. A.; Hulvat, J. F.; Stupp, S. I.; Hersam, M. C. Sorting Carbon Nanotubes by Electronic Structure Using Density Differentiation. *Nat. Nanotechnol.* **2006**, *1* (1), 60−65.

(5) Khripin, C. Y.; Fagan, J. A.; Zheng, M. Spontaneous Partition of Carbon Nanotubes in Polymer-Modified Aqueous Phases. *J. Am. Chem. Soc.* **2013**, *135* (18), 6822−6825.

(6) Subbaiyan, N. K.; Cambré, S.; Parra-Vasquez, A. N. G.; Hároz, E. H.; Doorn, S. K.; Duque, J. G. Role of Surfactants and Salt in Aqueous Two-Phase Separation of Carbon Nanotubes toward Simple Chirality Isolation. *ACS Nano* **2014**, *8* (2), 1619−1628.

(7) Zheng, M.; Jagota, A.; Semke, E. D.; Diner, B. A.; Mclean, R. S.; Lustig, S. R.; Richardson, R. E.; Tassi, N. G. DNA-Assisted Dispersion and Separation of Carbon Nanotubes. *Nat. Mater.* **2003**, *2* (5), 338−342.

(8) Wenseleers, W.; Cambré, S.; Čulin, J.; Bouwen, A.; Goovaerts, E. Effect of Water Filling on the Electronic and Vibrational Resonances of Carbon Nanotubes: Characterizing Tube Opening by Raman Spectroscopy. *Adv. Mater.* **2007**, *19* (17), 2274−2278.

(9) Takenobu, T.; Takano, T.; Shiraishi, M.; Murakami, Y.; Ata, M.; Kataura, H.; Achiba, Y.; Iwasa, Y. Stable and Controlled Amphoteric Doping by Encapsulation of Organic Molecules inside Carbon Nanotubes. *Nat. Mater.* **2003**, *2* (10), 683−688.

(10) Yanagi, K.; Miyata, Y.; Kataura, H. Highly Stabilized β-Carotene in Carbon Nanotubes. *Adv. Mater.* **2006**, *18* (4), 437−441.

(11) Gaufrès, E.; Tang, N. Y. W.; Lapointe, F.; Cabana, J.; Nadon, M. A.; Cottenye, N.; Raymond, F.; Szkopek, T.; Martel, R. Giant Raman Scattering from J-Aggregated Dyes inside Carbon Nanotubes for Multispectral Imaging. *Nat. Photonics* **2014**, *8* (1), 72−78.

(12) Cambré, S.; Campo, J.; Beirnaert, C.; Verlackt, C.; Cool, P.; Wenseleers, W. Asymmetric Dyes Align inside Carbon Nanotubes to Yield a Large Nonlinear Optical Response. *Nat. Nanotechnol.* **2015**, *10* (3), 248−252.

(13) Cambré, S.; Schoeters, B.; Luyckx, S.; Goovaerts, E.; Wenseleers, W. Experimental Observation of Single-File Water Filling of Thin Single-Wall Carbon Nanotubes Down to Chiral Index (5,3). *Phys. Rev. Lett.* **2010**, *104* (20), 207401.

(14) Cambré, S.; Wenseleers, W. Separation and Diameter-Sorting of Empty (End-Capped) and Water-Filled (Open) Carbon Nanotubes by Density Gradient Ultracentrifugation. *Angew. Chem., Int. Ed.* **2011**, *50* (12), 2764−2768.

(15) Fagan, J. A.; Huh, J. Y.; Simpson, J. R.; Blackburn, J. L.; Holt, J. M.; Larsen, B. A.; Walker, A. R. H. Separation of Empty and Water-Filled Single-Wall Carbon Nanotubes. *ACS Nano* **2011**, *5* (5), 3943−3953.

(16) Ma, X.; Cambré, S.; Wenseleers, W.; Doorn, S. K.; Htoon, H. Quasiphase Transition in a Single File of Water Molecules Encapsulated in (6,5) Carbon Nanotubes Observed by Temperature-Dependent Photoluminescence Spectroscopy. *Phys. Rev. Lett.* **2017**, *118* (2), 027402.

(17) Cambré, S.; Santos, S. M.; Wenseleers, W.; Nugraha, A. R. T.; Saito, R.; Cognet, L.; Lounis, B. Luminescence Properties of Individual Empty and Water-Filled Single-Walled Carbon Nanotubes. *ACS Nano* **2012**, *6* (3), 2649−2655.

(18) Chiashi, S.; Hanashima, T.; Mitobe, R.; Nagatsu, K.; Yamamoto, T.; Homma, Y. Water Encapsulation Control in Individual Single-Walled Carbon Nanotubes by Laser Irradiation. *J. Phys. Chem. Lett.* **2014**, *5* (3), 408−412.

(19) Tonkikh, A. A.; Rybkovskiy, D. V.; Orekhov, A. S.; Chernov, A. I.; Khomich, A. A.; Ewels, C. P.; Kauppinen, E. I.; Rochal, S. B.; Chuvilin, A. L.; Obraztsova, E. D. Optical Properties and Charge Transfer Effects in Single-Walled Carbon Nanotubes Filled with Functionalized Adamantane Molecules. *Carbon* **2016**, *109*, 87−97.

(20) Shi, L.; Rohringer, P.; Suenaga, K.; Niimi, Y.; Kotakoski, J.; Meyer, J. C.; Peterlik, H.; Wanko, M.; Cahangirov, S.; Rubio, A.; et al. Confined Linear Carbon Chains as a Route to Bulk Carbyne. *Nat. Mater.* **2016**, *15* (6), 634−639.

(21) Zhang, J.; Feng, Y.; Ishiwata, H.; Miyata, Y.; Kitaura, R.; Dahl, J. E. P.; Carlson, R. M. K.; Shinohara, H.; Tománek, D. Synthesis and Transformation of Linear Adamantane Assemblies inside Carbon Nanotubes. *ACS Nano* **2012**, *6* (10), 8674−8683.

(22) Talyzin, A. V.; Anoshkin, I. V.; Krasheninnikov, A. V.; Nieminen, R. M.; Nasibulin, A. G.; Jiang, H.; Kauppinen, E. I. Synthesis of Graphene Nanoribbons Encapsulated in Single-Walled Carbon Nanotubes. *Nano Lett.* **2011**, *11* (10), 4352−4356.

(23) Simon, J.; Flahaut, E.; Golzio, M. Overview of Carbon Nanotubes for Biomedical Applications. *Materials* **2019**, *12* (4), 624.

(24) Martincic, M.; Tobias, G. Filled Carbon Nanotubes in Biomedical Imaging and Drug Delivery. *Expert Opin. Drug Delivery* **2015**, *12* (4), 563−581.

(25) Perez Ruiz de Garibay, A.; Spinato, C.; Klippstein, R.; Bourgognon, M.; Martincic, M.; Pach, E.; Ballesteros, B.; Ménard-Moyon, C.; Al-Jamal, K. T.; Tobias, G.; Bianco, A. Evaluation of the Immunological Profile of Antibody-Functionalized Metal-Filled Single-Walled Carbon Nanocapsules for Targeted Radiotherapy. *Sci. Rep.* **2017**, *7* (1), 42605.

(26) Costa, P. M. F. J.; Sloan, J.; Rutherford, T.; Green, M. L. H. Encapsulation of RexOy Clusters within Single-Walled Carbon Nanotubes and Their *in Tubulo* Reduction and Sintering to Re Metal. *Chem. Mater.* **2005**, *17* (26), 6579−6582.

(27) Almadori, Y.; Alvarez, L.; Le Parc, R.; Aznar, R.; Fossard, F.; Loiseau, A.; Jousselme, B.; Campidelli, S.; Hermet, P.; Belhboub, A.; et al. Chromophore Ordering by Confinement into Carbon Nanotubes. *J. Phys. Chem. C* **2014**, *118* (33), 19462−19468.

(28) Gimenez-Lopez, M. d. C.; Chuvilin, A.; Kaiser, U.; Khlobystov, A. N. Functionalised Endohedral Fullerenes in Single-Walled Carbon Nanotubes. *Chem. Commun.* **2011**, *47* (7), 2116−2118.

(29) Kawai, M.; Kyakuno, H.; Suzuki, T.; Igarashi, T.; Suzuki, H.; Okazaki, T.; Kataura, H.; Maniwa, Y.; Yanagi, K. Single Chirality Extraction of Single-Wall Carbon Nanotubes for the Encapsulation of Organic Molecules. *J. Am. Chem. Soc.* **2012**, *134* (23), 9545−9548.

(30) Gaufrès, E.; Tang, N. Y. W.; Favron, A.; Allard, C.; Lapointe, F.; Jourdain, V.; Tahir, S.; Brosseau, C.-N.; Leonelli, R.; Martel, R. Aggregation Control of α-Sexithiophene *via* Isothermal Encapsulation inside Single-Walled Carbon Nanotubes. *ACS Nano* **2016**, *10* (11), 10220−10226.

(31) Yanagi, K.; Iakoubovskii, K.; Matsui, H.; Matsuzaki, H.; Okamoto, H.; Miyata, Y.; Maniwa, Y.; Kazaoui, S.; Minami, N.; Kataura, H. Photosensitive Function of Encapsulated Dye in Carbon Nanotubes. *J. Am. Chem. Soc.* **2007**, *129* (16), 4992−4997.

(32) van Bezouw, S.; Arias, D. H.; Ihly, R.; Cambré, S.; Ferguson, A. J.; Campo, J.; Johnson, J. C.; Defillet, J.; Wenseleers, W.; Blackburn, J. L. Diameter-Dependent Optical Absorption and Excitation Energy Transfer from Encapsulated Dye Molecules toward Single-Walled Carbon Nanotubes. *ACS Nano* **2018**, *12* (7), 6881−6894.

(33) Campo, J.; Piao, Y.; Lam, S.; Stafford, C. M.; Streit, J. K.; Simpson, J. R.; Hight Walker, A. R.; Fagan, J. A. Enhancing Single-Wall Carbon Nanotube Properties through Controlled Endohedral Filling. *Nanoscale Horizons* **2016**, *1* (4), 317−324.

(34) Wenseleers, W.; Vlasov, I. I.; Goovaerts, E.; Obraztsova, E. D.; Lobach, A. S.; Bouwen, A. Efficient Isolation and Solubilization of Pristine Single-Walled Nanotubes in Bile Salt Micelles. *Adv. Funct. Mater.* **2004**, *14* (11), 1105−1112.

(35) Stewart, J. J. P. Optimization of Parameters for Semiempirical Methods VI: More Modifications to the NDDO Approximations and Re-Optimization of Parameters. *J. Mol. Model.* **2013**, *19* (1), 1−32.

(36) Bondi, A. van der Waals Volumes and Radii. *J. Phys. Chem.* **1964**, *68* (3), 441−451.

(37) Streit, J.; Snyder, C. R.; Campo, J.; Zheng, M.; Simpson, J. R.; Hight Walker, A. R.; Fagan, J. A. Alkane Encapsulation Induces Strain in Small-Diameter Single-Wall Carbon Nanotubes. *J. Phys. Chem. C* **2018**, *122* (21), 11577−11585.

(38) Miyauchi, Y.; Saito, R.; Sato, K.; Ohno, Y.; Iwasaki, S.; Mizutani, T.; Jiang, J.; Maruyama, S. Dependence of Exciton Transition Energy of Single-Walled Carbon Nanotubes on Surrounding Dielectric Materials. *Chem. Phys. Lett.* **2007**, *442* (4), 394−399.

(39) Ando, T. Environment Effects on Excitons in Semiconducting Carbon Nanotubes. *J. Phys. Soc. Jpn.* **2010**, *79* (2), 024706.

(40) Silvera-Batista, C. A.; Wang, R. K.; Weinberg, P.; Ziegler, K. J. Solvatochromic Shifts of Single-Walled Carbon Nanotubes in Nonpolar Microenvironments. *Phys. Chem. Chem. Phys.* **2010**, *12* (26), 6990−6998.

(41) Jiang, J.; Saito, R.; Samsonidze, G. G.; Jorio, A.; Chou, S. G.; Dresselhaus, G.; Dresselhaus, M. S. Chirality Dependence of Exciton Effects in Single-Wall Carbon Nanotubes: Tight-Binding Model. *Phys. Rev. B: Condens. Matter Mater. Phys.* **2007**, *75* (3), 35407.

(42) Bachilo, S. M.; Strano, M. S.; Kittrell, C.; Hauge, R. H.; Smalley, R. E.; Weisman, R. B. Structure-Assigned Optical Spectra of Single-Walled Carbon Nanotubes. *Science* **2002**, *298* (5602), 2361−2366.

(43) Li, H.; Gordeev, G.; Garrity, O.; Peyyety, N. A.; Selvasundaram, P. B.; Dehm, S.; Krupke, R.; Cambré, S.; Wenseleers, W.; Reich, S.; Zheng, M.; Fagan, J. A.; Flavel, B. S. Separation of Specific Single-

Enantiomer Single-Wall Carbon Nanotubes in the Large-Diameter Regime. *ACS Nano* **2020**, *14* (1), 948−963.

(44) Cambré, S.; Wenseleers, W.; Goovaerts, E. Endohedral Copper(II)Acetylacetonate/Single-Walled Carbon Nanotube Hybrids Characterized by Electron Paramagnetic Resonance. *J. Phys. Chem. C* **2009**, *113* (31), 13505−13514.

(45) Schwan, H. P. Electrode Polarization Impedance and Measurements in Biological Materials. *Ann. N. Y. Acad. Sci.* **1968**, *148*, 191−209.

(46) Emmert, S.; Wolf, M.; Gulich, R.; Krohns, S.; Kastner, S.; Lunkenheimer, P.; Loidl, A. Electrode Polarization Effects in Broadband Dielectric Spectroscopy. *Eur. Phys. J. B* **2011**, *83* (2), 157.